



Enhanced toluene sensing performances of Pd- loaded SnO₂ cubic nanocages with porous nanoparticle-assembled shells



Liang Qiao^a, Yifei Bing^b, Yanzhe Wang^b, Shansheng Yu^b, Zhongzhu Liang^{c,*}, Yi Zeng^{b,*}

^a College of Science, Changchun University, Changchun 130022, PR China

^b College of Materials Science and Engineering, State Key Laboratory of Automotive Simulation and Control, and Key Laboratory of Automobile Materials of Ministry of Education (MOE), Jilin University, Changchun 130012, PR China

^c State Key Laboratory of Applied Optics, Changchun Institute of Optics, Fine Mechanics and Physics, Chinese Academy of Sciences, Changchun 130033, PR China

ARTICLE INFO

Article history:

Received 15 March 2016

Received in revised form 7 September 2016

Accepted 6 October 2016

Available online 6 October 2016

Keywords:

SnO₂

Nonspherical hollow structures

Pd loading

Toluene

Gas sensor

ABSTRACT

Pure and Pd-loaded SnO₂ cubic nanocages with hierarchically nanoparticle-assembled and porous shells have been successfully fabricated through a straightforward multi-step route. The synthetic step-dependent structure evolution and the formation mechanism have been discussed. Furthermore, the toluene-sensing performances of these Pd-loaded SnO₂ nanocages are elaborated and compared with those of pure SnO₂. The toluene sensing results demonstrate that Pd-loaded SnO₂ nanocages with the optimal loading amount of 1.0 mol% show a low detection limit (0.1 ppm) with response of 41.4–20 ppm toluene at the working temperature of 230 °C with the fast response time of 0.4 s, and improved selectivity. The improvement of toluene sensing properties is not only attributed to the effective utility of hollow and porous architecture, but also due to the dramatic sensitization of the loaded Pd nanoparticles.

© 2016 Elsevier B.V. All rights reserved.

1. Introduction

Owing to the increasing concerns of air pollution from harmful or toxic gases in recent years, research on preparation and engineering of sensing materials for gas monitoring and detection has become a hot topic [1,2]. Toluene (C₇H₈) is one of the most dangerous air pollutants from its wide applications as diluents, adhesive in interior decoration and automotive interior parts, which is very closely related to our daily lives and eventually leads to severe damages on human health through long-term high concentration contact [3]. Although much progress has been made on toluene detection, it is endless for researchers to seek higher toluene sensing performances to meet the increasing needs and more complex application circumstances.

Semiconducting oxides such as SnO₂, ZnO and TiO₂ have been prepared and explored for toluene detection [4–8]. Among the potential candidates, SnO₂, as a versatile wide bandgap semiconductor ($E_g = 3.6$ eV, $T = 300$ K), has attracted considerable attention due to the low-cost and green synthesis and extensive applications in detecting many kinds of gases [9–15]. Since the general sensing principle of semiconducting oxides is decided by the signif-

icant difference of electrical characteristics when they are exposed to air or testing gases, maintaining a less-agglomerated configuration and high surface area of the oxides is advantageous to improve the gas-sensing performances [16]. In this respect, hollow nanostructures functionalized with shell materials have been recognized as one type of desirable configurations, which not only exhibit less-agglomerated structure with outer/inner surfaces for high specific surface area but also facilitate the fast mass transfer of gas molecules to adsorb and desorb from the surfaces. So far different hollowing strategies have been successfully applied to construct various SnO₂ hollow particles, which obviously exhibit the improved sensing properties to different sorts of gases compared with the achievement of their solid counterparts [13–15].

As far as the amelioration of gas-sensing performances is concerned, many efforts have been concentrated on the tailoring of specific surface area and surface accessibility through controlling their structure, phase, shape, and size. However, selectivity of pure SnO₂ to different gases, especially those having similar physicochemical properties, gets little benefit from high surface areas due to simultaneous reaction with several gas species. Fortunately, the intended addition of noble metals or other impurities may be an alternative but more effective strategy through dramatically promoting the electrochemical reaction with target gas or introducing intrinsically different impurity levels into the sensing process [17]. Among various noble metals, Pd is one of the most used catalysts for

* Corresponding authors.

E-mail addresses: liangzz@ciomp.ac.cn (Z. Liang), zengyi@jlu.edu.cn (Y. Zeng).

the significant improvement of gas-sensing performances [18–24]. For instance, Yamazoe and Lee et al. [17,20] found that Pd-doped SnO_2 nanorod thin films show distinctly enhanced H_2 sensing properties. Korotcenkov et al. [21] reported that surface Pd doping of SnO_2 thin films exhibit the improved CO sensing performances. Vaishampayan et al. [22] found that the loaded Pd particles promote response of the sensors based on SnO_2 nanospheres towards liquid petroleum gas (LPG). Zhang et al. [23] reported the enhanced H_2 sensing behaviors based on Pd- SnO_2 nanofibers. Choi et al. [24] reported the fast response and recovery capacity of SnO_2 nanowires functionalized by bimetallic Pd/Pt nanoparticles for NO_2 detection.

In this work, we report a low cost and environmental-friendly multistep route for pure and Pd-loaded SnO_2 cubic nanocages without employing any additional templates, surfactants or capping agents. The crystallinity, morphology, and structure characteristics of the as-prepared products are investigated, and the results demonstrate that pure and Pd-loaded SnO_2 products have cubic shape with hierarchically nanoparticle-assembled and porous shells. The possible mechanism of these non-spherical hollow structures is also discussed via the elaboration of the synthetic step-dependent evolution process. Furthermore, the significantly enhanced toluene sensing properties of Pd-loaded SnO_2 nanostructure are also investigated as a function of the content of Pd.

2. Experimental procedures

2.1. Synthesis and characterization of pure and Pd-loaded SnO_2 cages

All the reagents are of analytical grade and purchased from Shanghai Chemical Reagent Factory, and used without further purification. Unloaded SnO_2 hollow cages were synthesized by following our previous strategy with elaborate modification [15]. The typical synthetic route involves a three-step procedure. Briefly, (1) 40 mL of aqueous solution including ZnCl_2 (0.025 M), $\text{SnCl}_4 \cdot 5\text{H}_2\text{O}$ (0.025 M), and NaOH (11 mmol) was prior prepared under vigorous stirring until a uniform suspension was formed and aging for 2 h. Another 20 mL NaOH was subsequently added dropwise into the above solution under vigorous stirring. The white precipitates were then centrifuged and washed with absolute ethanol/deionized water for several times, prior to drying to get the precursors. (2) The collected samples were annealed at 850 °C for 30 min to obtain the annealed samples. (3) The annealed samples (50 mg) were then dispensed in HNO_3 solution (8 M) for 8 h and the remainders were centrifuged, washed and dried in air to get the pure SnO_2 products.

For Pd-loaded SnO_2 products, 10 mL of aqueous solution including the obtained SnO_2 products and appropriate quantity of PdCl_2 (molar ratio was 0.5 mol%, 1.0 mol%, and 1.5 mol%, respectively) was prepared under incessantly vigorous stirring. Then, ammonia solution was added dropwise into the above aqueous solution under vigorous stirring until the pH level was controlled to approximately 10. The precipitates were centrifuged, washed for several times, dried in air. Finally, the dried samples were collected to anneal at 350 °C for 1 h and cooled down naturally to obtain the final Pd-loaded SnO_2 products.

The as-prepared products were characterized by powder X-ray diffraction (XRD, Rigaku D/max-2550) with Cu K α radiation ($\lambda = 0.15418 \text{ nm}$), field emission scanning electron microscope (FESEM, FEOL JSM-6700F, 8 kV), transmission electron microscope (TEM), selected-area electron diffraction (SAED), and high-resolution TEM (HRTEM, JEOL JEM-2100F, 200 kV), respectively. The surface area properties of sample were measured through measuring nitrogen adsorption-desorption isotherms with a Micrometrics ASAP2020 apparatus, and the pore size distri-

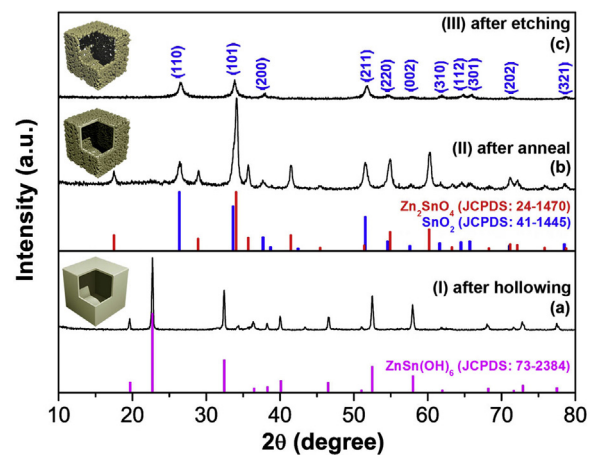


Fig. 1. XRD patterns of the obtained products after different treatments: (a) co-precipitation, (b) anneal, and (c) etching process, respectively.

bution was obtained by Barrett-Joyner-Halenda (BJH) method from the desorption branch of isotherms.

2.2. Fabrication and measurement of gas sensing properties

The obtained SnO_2 products were mixed with deionized water in a weight ratio of 4:1 to form a slurry, which then was pasted uniformly on the surface of a Si-based platform with prefabricated Au signal electrodes and a heater to form a direct-heated thick sensing film with a thickness of about 0.1 mm. The schematic structure of the gas sensor and the detailed fabrication process of Si-based gas sensor have been described elsewhere [25]. The desired concentrations of the testing gases are obtained by the static liquid gas distribution method and the gas-sensing properties of SnO_2 samples are measured with a WS-60A gas-sensing characterization system (Weisheng Instruments Co. Ltd. China). The response (R) of gas sensor is defined as the ratio (R_a/R_g) of the resistance of the sensor in dry air (R_a) to that in the testing gas (R_g). The response time (τ_{res}) and recovery time (τ_{recov}) are defined as the time taken by the sensor to achieve 90% of the total resistance change in the case of adsorption and desorption, respectively.

3. Results and discussion

3.1. Structural and morphological characteristics

The crystallinity and phase information of all the obtained products have been identified by XRD measurements. Firstly, XRD patterns of products corresponding to different steps before the Pd-loaded treatment are shown in Fig. 1. XRD pattern of the products obtained via the room-temperature co-precipitation process is shown in Fig. 1a. All the diffraction peaks agree perfectly with the corresponding peaks of standard $\text{ZnSn}(\text{OH})_6$ (Zinc hydroxystannate, ZHS) phase (JCPDS card no. 73-2384) and no peaks of other crystalline phases are observed. After the anneal process, all the diffraction peaks of the middle XRD pattern (Fig. 1b) can be discriminated and indexed to two sets of standard diffraction patterns, which are composed of tetragonal rutile SnO_2 (JCPDS card No. 41-1445) and cubic inverse spinel Zn_2SnO_4 (JCPDS card No. 24-1470). It suggests that ZHS products are decomposed completely during the anneal process at 850 °C in air. As for the etched products, all the diffraction peaks can be indexed to tetragonal SnO_2 (JCPDS card No. 41-1445), indicating that Zn_2SnO_4 phase dissolves and finally disappears from the $\text{Zn}_2\text{SnO}_4/\text{SnO}_2$ hybrids while SnO_2 phase remains (Fig. 1c). Obviously, there is broadening and descending trend in the intensity of peaks with the advance of experimental proce-

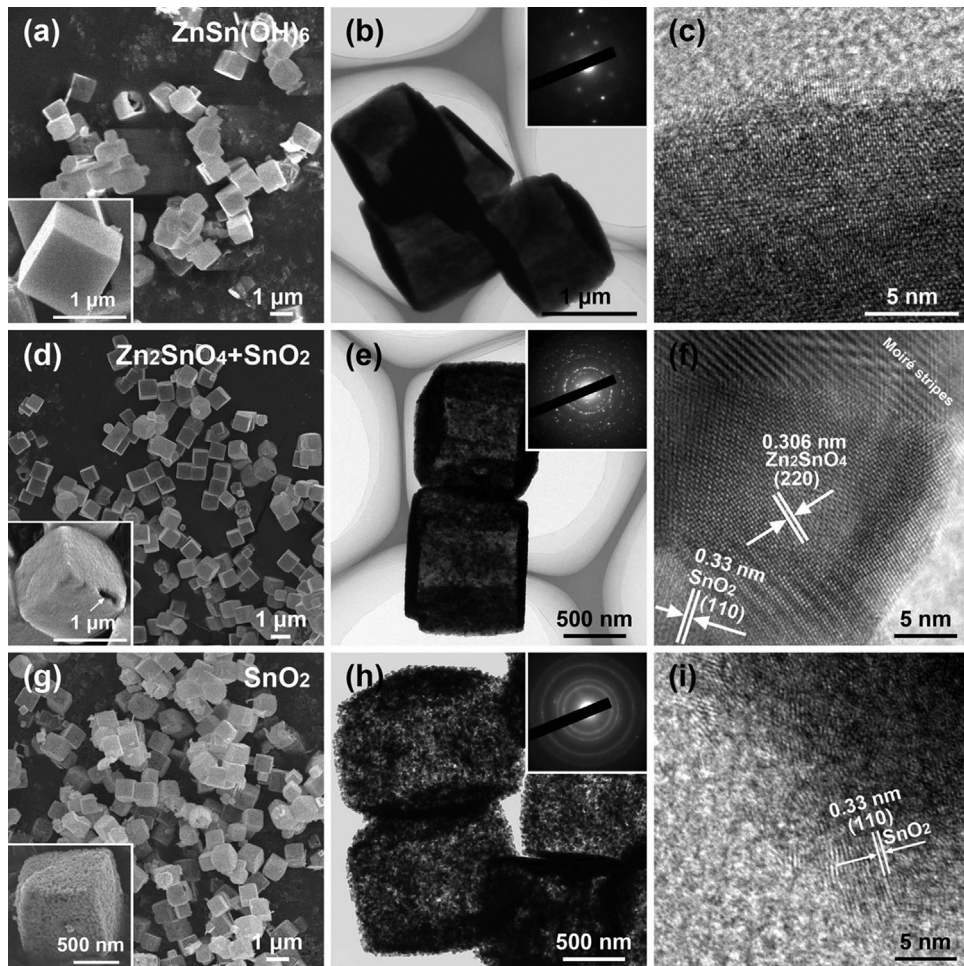


Fig. 2. (a) FESEM, (b) TEM, (c) HRTEM images and the corresponding SAED inset of ZHS cubic cages; (d) FESEM, (e) TEM, (f) HRTEM images and the corresponding SAED inset of hybrid $\text{SnO}_2/\text{Zn}_2\text{SnO}_4$ cages; (g) FESEM, (h) TEM, (i) HRTEM images and the corresponding SAED inset of pure SnO_2 cages. Insets of (a), (d) and (g) are the typical FESEM images of a single box, respectively.

dure, which can be confirmed through the enlargement of (110), (101) and (211) peaks of SnO_2 from different synthetic stages. It demonstrates that the undoped SnO_2 products will inherit the composition from $\text{SnO}_2/\text{Zn}_2\text{SnO}_4$ products and etching decreases the crystallite size of SnO_2 .

The typical morphology and microstructures of the products belonged to different stages are characterized via FESEM and TEM observation. As can be seen from Fig. 2a and its inset, it confirms that the as-obtained ZHS products are composed of monodisperse particles with well-shaped cubic appearance and smooth surfaces and the general length is in the range of 600–900 nm. The typical TEM image in Fig. 2b indicates that these ZHS cubes actually possess single-shelled hollow structure by the obvious light contrast between the dark edges and the relatively pale cavity and the thickness of the wall is in the range of about 75–95 nm. The inserted SAED pattern in Fig. 2b exhibits a set of diffraction spots with a square symmetry, which indicates that ZHS cages are composed of six equivalent shells. As shown in Fig. 2c, HRTEM image of the edge area of one ZHS box reveals the parallel and regular lattice fringes. Combining with the SAED pattern, it can provide direct evidences for single-crystalline nature of the cubic ZHS cages. As shown in Fig. 2d, low-magnification FESEM image indicates that although there is a large change in crystalline phases during the anneal treatment, the shape and size of $\text{SnO}_2/\text{Zn}_2\text{SnO}_4$ hybrids are well inherited from ZHS cages. As shown in the inset of Fig. 2d, the cubic shape and hollow interior with obvious rough planes

of $\text{SnO}_2/\text{Zn}_2\text{SnO}_4$ products can be observed from the individual box with partly broken edge. Fig. 2e shows a representative TEM image of $\text{Zn}_2\text{SnO}_4/\text{SnO}_2$ cages and the single-shelled structure with hollow interior can be clearly discerned. As shown in the inset of Fig. 2e, the corresponding SAED pattern exhibits some diffraction rings with complex features, which can be differentiated to two sets of polycrystalline structures in nature, including tetragonal SnO_2 and cubic inverse spinel Zn_2SnO_4 . Furthermore, from the HRTEM image (Fig. 2f), it is demonstrated that hybrid cages are composed of a large quantity of nanometer-sized particles, where these clear interplanar spacings of 0.306 nm and 0.33 nm correspond to the Zn_2SnO_4 (220) and SnO_2 (110) planes, respectively. Furthermore, the HRTEM image also shows indistinct Moiré stripes, which could be ascribed to the overlapping of crystal lattices of Zn_2SnO_4 and SnO_2 crystallites with different crystallographic directions. As shown in Fig. 2g, a panoramic view reveals that pure SnO_2 products consist of hollow particles with entirely uniform cubic shape and rougher shells. As shown in inset of Fig. 2g, the detailed view on an individual SnO_2 cube confirms that many neighboring primary nanoparticles aggregate together to form hierarchical SnO_2 cages with a uniform size of about 10–15 nm. More structural characteristics of cubic SnO_2 particles are further elucidated by TEM and HRTEM. Fig. 2h gives a typical low-magnification TEM image and the results not only exhibit a high uniformity of the cubes, in agreement with the above FESEM observations, but also show an obvious hierarchical structure with nanoparticles as build-

ing blocks. After the Zn_2SnO_4 phase segregation process, SnO_2 would aggregate and further crystallize to form single-crystalline subunits while numerous micro- and mesopores remain to form three-dimensional network along the high-curvature edges or the path of dissolution of Zn_2SnO_4 phase in the Zn_2SnO_4/SnO_2 hybrids. Furthermore, the lattice interplanar spacing of a subunit nanoparticle is determined to be 0.33 nm, corresponding to the (110) planes of the rutile SnO_2 (Fig. 2i). Combining with the ring-like pattern from SAED analysis (inset of Fig. 2h), the short-range order and overlap of lattice fringes demonstrate that the crystallographic axes of all particles are randomly oriented, providing direct evidence for the polycrystalline texture in nature.

In addition, the XRD patterns of Pd-loaded SnO_2 with different amounts (0 mol%, 0.5 mol%, 1.0 mol% and 1.5 mol%) are also shown in Fig. 3a. From careful examination, one can confirm that no peaks corresponding to Pd, PdO_x or other crystalline phases are observed. Compared to the diffraction peaks of pure SnO_2 being well matched with that of standard rutile SnO_2 (JCPDS card No. 41-1445), the discernible shift in the position of the same (101) and (200) diffraction peaks can be observed in Fig. 3b, exhibiting a trend toward high angles with increasing amount of loaded Pd. Typically, the existence of Pd component in Pd-loaded SnO_2 samples is investigated via XPS spectrum on the as-prepared 1.0 mol% Pd-loaded SnO_2 . As shown in Fig. 3c, the peaks at binding energies of ~495 eV and ~486 eV can be attributed to $Sn\ 3d_{3/2}$ and $3d_{5/2}$, respectively. The upper inset of Fig. 3c exhibits the asymmetric O 1s spectra, which can be fitted by two peaks with binding energies at 531.9 eV and 530.4 eV, respectively. The peak at 531.9 eV can be characteristic of surface-absorbed oxygen species (i.e., O_2^- and O^-) and another peak at 530.4 eV could be regarded as typical surface lattice oxygen [26]. In addition, the Pd 3d spectra is shown in the lower inset of Fig. 3c, and it presents that the peaks at 341.8 eV for Pd 3d_{3/2} and 336.6 eV for Pd 3d_{5/2} are in agreement with the values for PdO , which confirm that a majority of Pd atoms in the as-prepared samples are present as PdO surface species [23], and probably small mole percent results in weak Pd (PdO) peaks of XRD overlapping the SnO_2 peaks.

In addition, FESEM observations of Pd-loaded SnO_2 products with different loading concentrations are shown in Fig. 4. As shown in Fig. 4a, we can find that the unloaded SnO_2 products are composed of monodisperse cages with hierarchical nanoparticle-assembled and obvious porous shells. Then Fig. 4b-d show the FESEM images of Pd-loaded SnO_2 products with Pd loading concentrations of 0.5 mol%, 1.0 mol%, and 1.5 mol%, respectively. From careful examination, one can find that all the Pd-loaded SnO_2 cages in fact exhibit the same and uniform shape to the pure SnO_2 cages. Although they have subtle differences on the stability, meaning the increasing fragments from broken cages with the increase of Pd loading concentration, the sizes of nanoparticles of these loaded SnO_2 cages are almost the same as that of the pure samples. According to the morphological and structural evolution of the as-obtained products, the formation of final Pd-loaded SnO_2 cages with hierarchical nanoparticle-assembled and porous shells is illustrated in Fig. S1 (Supplementary materials). The rational assembly of Pd-loaded SnO_2 cages for application in gas sensor is inspired by understanding of the key parameters and mechanism for the production of double-shelled SnO_2 nanocages in our previous work [15]. Obviously, the formation process can be separated into four distinct purposeful steps. Firstly, ZHS cubic cages with controllable shell thickness can be constructed via an aging time-dependent hollowing evolution, where the initial co-precipitation products of monodisperse ZHS solid cubes serve as not only the starting materials, but also the site of sacrificial self-templates. As shown, ZHS is one of perovskite oxides with face-centered-cubic (FCC) closed packing and the surface energies of different crystal planes show a relative order as follows: $\gamma\{111\} < \gamma\{100\} < \gamma\{110\}$ [27,28]. ZHS

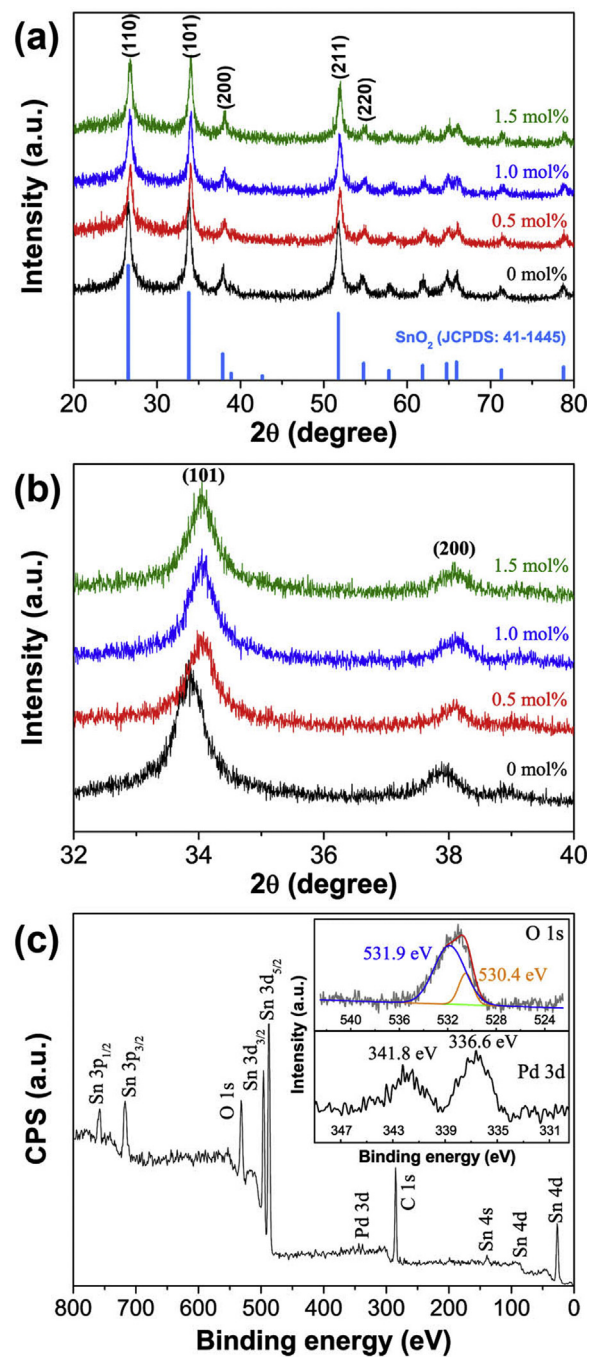


Fig. 3. (a) XRD patterns of Pd-loaded SnO_2 with different Pd loading concentrations, (b) the enlarged XRD patterns in the range of 32–40°, (c) XPS spectra of 1.0 mol% Pd-loaded SnO_2 sample. The upper and lower insets of Fig. 3c are the corresponding high-resolution O 1s and Pd 3d spectra, respectively.

particles with specific shape and size can be obtained as a result of the fast co-precipitation reaction following the intrinsic growth habit of FCC closed packing and amount of NaOH. In this study, cubic ZHS crystals are obtained via control of the appropriate amount of NaOH (11 mmol) and subsequent Ostwald ripening for their corresponding hollow counterparts. Then the preparation of SnO_2 cubic cages with nanoparticle-assembled and porous shells can be obtained through an anneal-etching strategy, which is related to the anneal step for phase transition from ZHS to Zn_2SnO_4/SnO_2 hybrids and etching step for selective evacuation of Zn_2SnO_4 to obtain pure SnO_2 particles. Finally, Pd nanoparticles are formed and eventually loaded on the porous shells of SnO_2 particles through

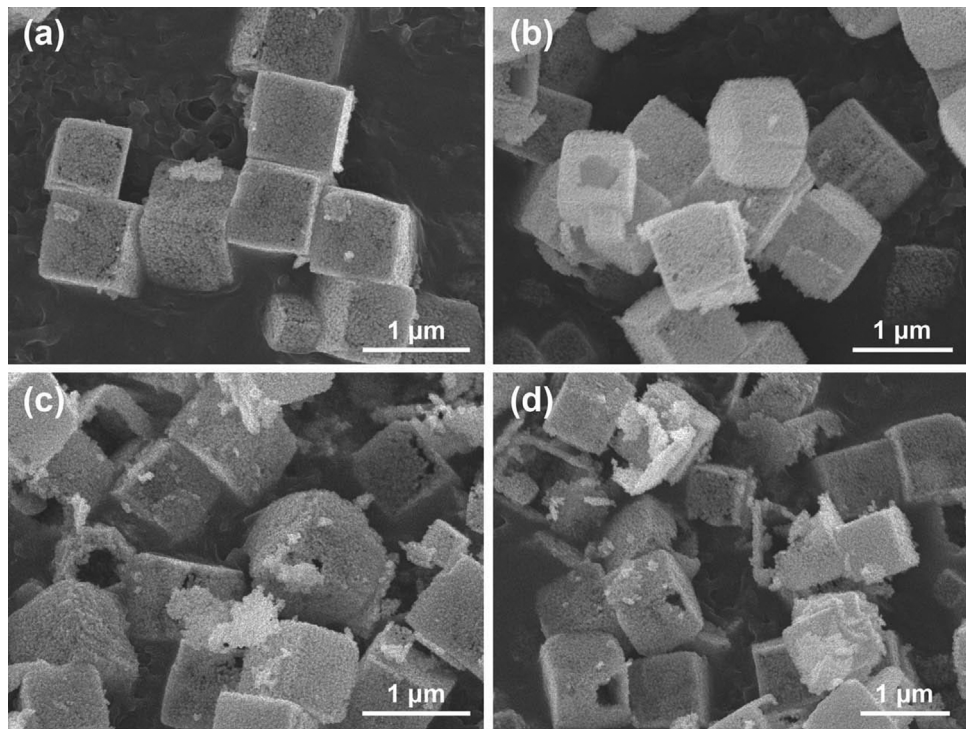


Fig. 4. FESEM images of Pd-loaded SnO_2 cages with different loading concentration: (a) 0 mol%, (b) 0.5 mol%, (c) 1.0 mol%, and (d) 1.5 mol%.

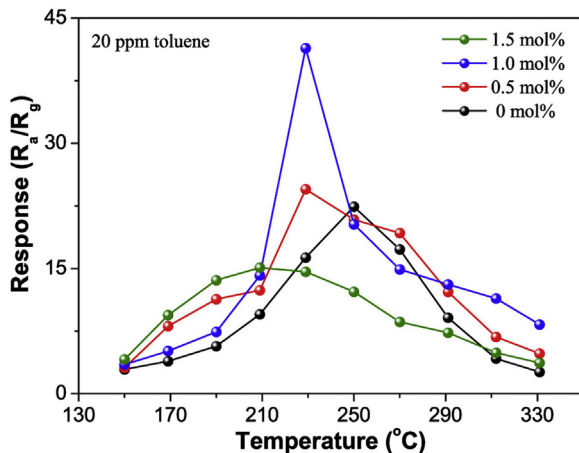


Fig. 5. Response versus operating temperature of Pd-loaded SnO_2 cages with different Pd concentrations to 20 ppm toluene.

last purposeful step, which is inspired by the significant improvement of gas-sensing behaviors based on Pd nanoparticles.

3.2. Toluene-sensing properties and mechanism

For the sensor based on semiconducting oxides to a given gas species, the appropriate working temperature is an important factor to obtain the optimal gas-sensing performances, which is determined essentially by the dynamic equilibrium between the speed of the chemisorbed reaction and the diffusion speed of gas molecules [29]. In order to obtain the optimal working temperature of our sensors for toluene detection, the responses of sensors based on unloaded and Pd-loaded SnO_2 cages to 20 ppm toluene have been investigated as a function of working temperature. As shown in Fig. 5, it can be observed that the response values of sensors based on different SnO_2 products vary with the operating temperature in the range of 150–330 °C. As for unloaded SnO_2 sensor, the

varied response values with operating temperature demonstrate that the response increases with the increasing operating temperature and reaches its maximum, and then gradually decreases with further increasing temperature from 250 °C to 330 °C. In addition, this tendency is commonly observed from other SnO_2 sensors, but the optimum operating temperatures have a slight shift toward the decreased temperature as Pd addition increases from 0 mol% to 1.5 mol%. Specifically, it can be observed that unloaded SnO_2 sensor exhibits the highest response of 22.1 at 250 °C and the maximum values of Pd-loaded SnO_2 with 0.5 mol%, 1.0 mol%, and 1.5 mol% Pd additions are 24.5, 41.4, and 15.1, respectively. Therefore, Pd-loaded SnO_2 products with the optimal working temperature and Pd addition will be further applied to all the gas-sensing investigations hereinafter.

The relationship between response of sensor based on 1.0 mol% Pd-loaded SnO_2 products and toluene concentration is illustrated in Fig. 6. For comparison, toluene sensing performances of sensor based on unloaded SnO_2 products are exhibited simultaneously. The results demonstrate that the response values of all sensors increase with the increased toluene concentration, but the increasing tendency of Pd-loaded SnO_2 is obviously faster than that of unloaded SnO_2 until the concentration increases to 400 ppm with sensors tending to saturation thereafter. Interestingly, response of Pd-loaded SnO_2 sensor is approximately linear as toluene concentration is less than 40 ppm. As shown in inset of Fig. 6, the distinguishable lowest concentration from Pd-loaded SnO_2 sensor is 0.1 ppm with the response value of 1.15 while the lowest detecting concentration of unloaded SnO_2 is 1 ppm with the response value of 1.4, which verifies the promotional effect of Pd nanoparticles.

In order to corroborate the argument that the improved sensing performance is attributed more to the loaded Pd rather than the unique hollow configuration, the nitrogen adsorption-desorption isotherms and pore size distribution curves (inset) of unloaded and 1.0 mol% Pd-loaded SnO_2 cages are shown in Fig. 7, respectively. As shown in Fig. 7a, the unloaded SnO_2 nanocages have type IV nitro-

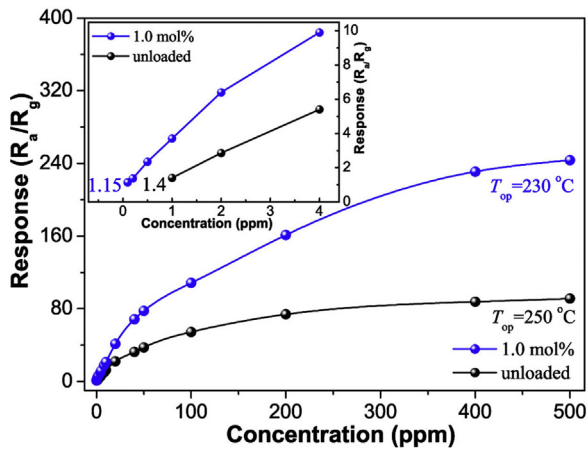


Fig. 6. Response curves of unloaded and 1.0 mol% Pd-loaded SnO₂ products to various toluene concentrations, respectively. The inset shows a quasi-linear dependence of the response of different SnO₂ on toluene concentration within 0.1–4 ppm.

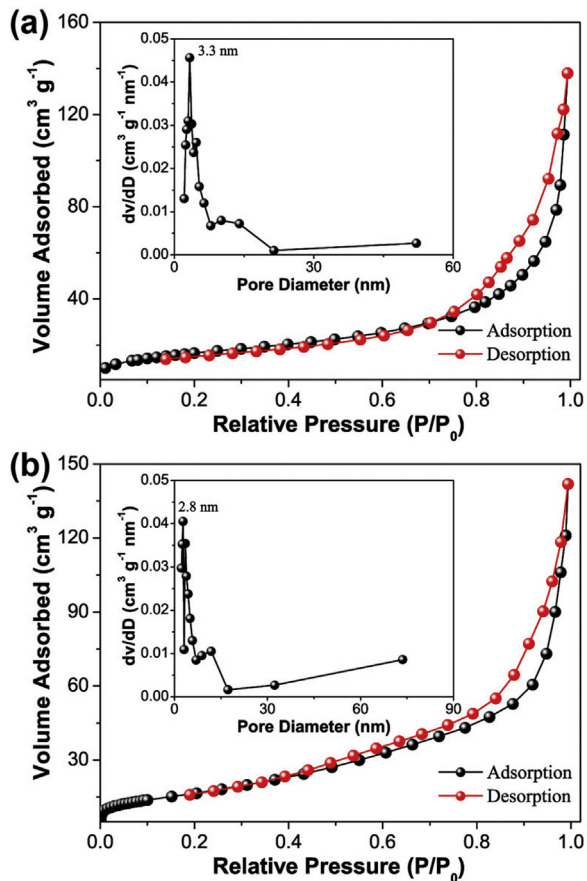


Fig. 7. Nitrogen adsorption and desorption isotherms of (a) unloaded SnO₂ nanocages and (b) 1.0 mol% Pd-loaded SnO₂ nanocages with their corresponding pore-size distribution (inset) calculated by BJH method from desorption branch.

gen adsorption and desorption isotherms and the corresponding Brunauer–Emmett–Teller (BET) specific surface area is calculated to be 89 m² g⁻¹. Using the BJH method and the desorption branch of the nitrogen isotherm, the calculated pore-size distribution indicates that the material contains an average pore size of 12.4 nm and a maximum at 3.3 nm, indicating the highly macro- and mesoporous nature of shells from unloaded SnO₂. As shown in Fig. 7b, the BET surface area of 1.0 mol% Pd-loaded SnO₂ cages is calculated to be 71.3 m² g⁻¹, exhibiting a slightly lower surface area than that

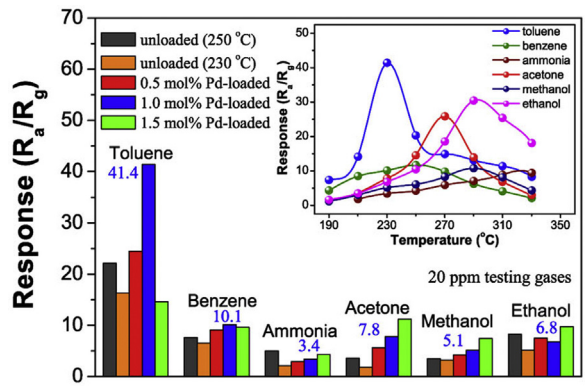


Fig. 8. Selectivity of sensors based on pure and Pd-loaded SnO₂ to 20 ppm various testing gases. The inset shows the response of 1.0 mol% Pd-loaded SnO₂ cages versus operating temperature to 20 ppm different gases.

of pure SnO₂ cages. Furthermore, the inset pore-size distribution curve exhibits that Pd-loaded SnO₂ cages contain an average pore size of 24.9 nm with a maximum at 2.8 nm, which is also bigger than that of unloaded SnO₂ cages. Thus, the results demonstrate that the loading of Pd nanoparticles has not too much to destroy the mesoporous structure, indicating that the loaded SnO₂ with optimal Pd addition still maintains the similar local microenvironment for chemical mixing and mass transport. It also indicates that the improved sensing properties are further ascribed to the introduction of Pd.

Furthermore, selective detection of a target gas among different interfering gases, especially those having similar physicochemical properties, is very important in the practical applications. Therefore, the selective histogram of sensors based on unloaded and Pd-loaded SnO₂ has also been tested to different gases. As shown in Fig. 8, the responses of all the sensors to 20 ppm toluene are all higher than their responses to other testing gases with the same concentration. Compared with the sensors based on unloaded SnO₂ and those Pd-loaded SnO₂ with Pd additions of 0.5 mol% and 1.5 mol%, the 1.0 mol% Pd-loaded SnO₂ exhibit obvious advantages in selective detection of toluene at low working temperature of 230 °C. Specifically, it can be observed that 1.0 mol% Pd-loaded SnO₂ sensor exhibits the highest response value of 41.4–20 ppm toluene, which is almost four times higher than the obtained response (10.1) of the sensor to benzene and more times higher than that to other potential interfering volatile organic compounds (VOCs), such as methanol, acetone, and ethanol. Meanwhile, compared with the responses of different Pd-loaded SnO₂ sensors to these gases at 230 °C, much lower response but similar selective character is obtained from unloaded SnO₂ sensor under the same testing process with different operating temperature of 230 °C and 250 °C. It is reasonable to conclude that 1.0 mol% Pd addition in SnO₂ nanocages is an efficient route to improve selectivity and response to toluene. A comparison about the sensing capacity of 1.0 mol% Pd-loaded SnO₂ sensor to these gases is displayed in the inset of Fig. 8. The results demonstrate that different gases have different optimum working temperatures, which is in favor of considering the different potential applications.

The dynamic response and recovery characteristic, as another important aspect of gas-sensing performance, has also been investigated. Fig. 9a presents several dynamic and continuous response-recovery periods of 1.0 mol% Pd-loaded SnO₂ sensor to toluene with the incremental concentration from 1 to 20 ppm. The response values to 1, 2, 5, 10, and 20 ppm toluene are 3.7, 6.4, 11.8, 21.2, and 41.4, respectively. As shown in insets of Fig. 9a, the typical τ_{res} and τ_{recov} of Pd-loaded SnO₂ sensor to 20 ppm toluene are 0.4 and 16.5 s, respectively. Fig. 9b presents the τ_{res} and τ_{recov} of Pd-

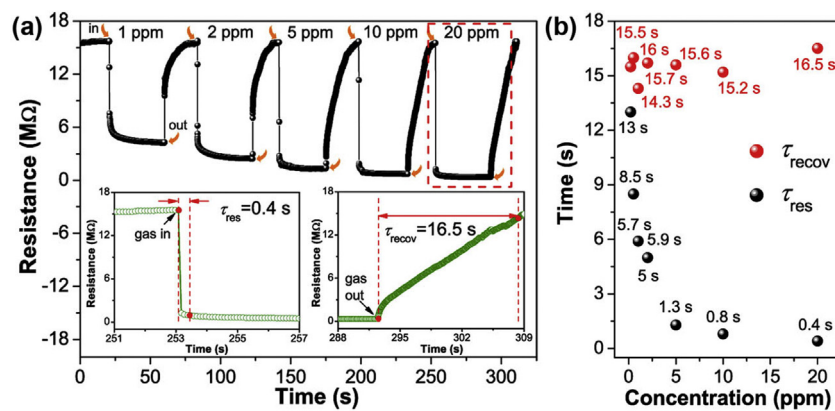


Fig. 9. (a) Dynamic toluene sensing transients of 1.0 mol% Pd-loaded SnO₂ cages to toluene with the increasing concentration. The insets show the corresponding response time (τ_{res}) and recovery time (τ_{recov}) of Pd-loaded SnO₂ cages to 20 ppm toluene. (b) Response-recovery time of Pd-loaded SnO₂ cages to 0.2–20 ppm toluene.

Table 1

Comparison between Pd-loaded SnO₂ cubic cages in the present work and other SnO₂-based nanostructures.

Materials	Temperature (°C)	Response	Detection limit (ppm)	Response-recovery times(s)	Reference	
Pd-loaded SnO ₂ cubic cages	230	41.4 (20 ppm)	0.1	0.4	16.5	This work
SnO ₂ -ZnO hollow nanofibers	190	15.6 (50 ppm)	1	6–11	12–23	[6]
Pd-loaded flowerlike SnO ₂	250	17.4 (10 ppm)	0.08	~10	>400	[7]
double-shelled SnO ₂ cages	250	33.4 (20 ppm)	1	2.3	5.8	[15]
NiO-SnO ₂ nanofibers	330	11 (50 ppm)	50	11.2	4	[30]
meso-macroporous SnO ₂	220	3 (100 ppm)	10	5	38	[31]
SnO ₂ nanofibers	350	9 (200 ppm)	10	1	5	[32]

loaded SnO₂ sensor to toluene with the concentration in the range of 0.2–20 ppm. The results indicate that the τ_{res} values are dramatically decreased from 13 s (0.2 ppm) to 0.4 s (20 ppm), whereas the corresponding τ_{recov} values are much longer and relatively stable (14.3–16 s) than that of the response time. Compared with toluene sensing performances of other SnO₂-based sensors, as summarized in Table 1 [6,7,15,30–32], our Pd-loaded SnO₂ cages show obvious response to low concentration of toluene and shorten response time. The extremely fast response behaviors of 1.0 mol% Pd-loaded SnO₂ cages can be attributed to the unique nanoparticle-assembled and porous structures and the effects of Pd loading, which not only provide diffusion channels for fast mass transfer of gas molecules to reach or leave the sensing surfaces, but also dramatically promote the electrochemical reaction with target gas or introduce intrinsically different impurity levels into the sensing process, resulting in the high response and fast response.

When Pd is brought to an intimate contact with SnO₂, a constant Fermi level will be achieved throughout the interface, which is in thermal equilibrium with respect to the Pd-loaded SnO₂ system (Fig. 10a). As the work function of Pd (Φ_{Pd} , 5.6 eV) is larger than that of SnO₂ (Φ_{SnO_2} , 4.5 eV), electrons in SnO₂ will transfer to Pd and there exists a strong tendency for the valence and conduction bands of SnO₂ to upward bending, especially around the interface region of SnO₂ with Pd. As a consequence, the modulation of this barrier is beneficial to the formation of depletion zones around SnO₂ and the improved sensing performance is anticipated. Concerning the sensing process and mechanism of SnO₂ nanocages for toluene, it can be derived from the change of electrical conductance caused by surface-controlled charge transfer in different ambiances [33,34]. When SnO₂ sensor is exposed to air, due to a stronger electron affinity, oxygen molecules can be adsorbed on the surface of SnO₂ nanostructures and trap electrons from the conduction band of SnO₂ to form oxygen species (O₂[−], O[−], or O^{2−}). This process decreases the electronic concentration to form a thick depletion layer around the surface regions of SnO₂ and eventually results in a stable high resistance of sensor (Fig. 10b and d). When

SnO₂ sensor is exposed to reducing gas ambience (like toluene) with a feasible temperature, these adsorbed oxygen species would react with toluene molecules to release the trapped electrons back to the conduction band. This process decreases the width of the surface depletion layer and eventually results in a low resistance of SnO₂ sensor (Fig. 10c and e). Subsequently, when SnO₂ sensor is exposed to air again, oxygen molecules can re-adsorb on SnO₂ surface and the sensor restores its original high resistance to complete a whole response-recovery period.

Based on the basic sensing principle, Yamazoe et al. outline the design principle of high-performance gas sensing materials [2]. The improved toluene-sensing performances of SnO₂ products observed here are most likely to be ascribed to the following aspects: (i) nonspherical SnO₂ hollow nanocages exhibit a reasonable configuration with the nanoparticle-assembled and porous hollow architecture, which not only maintains high specific surface area but also provides penetrable shells with various macropores and mesopores for surface accessibility [16]. The BET results and their corresponding pore-size distributions (Fig. 7) explicitly verify that hollow cubic structures possess a satisfying form without sacrificing high surface area and surfactivity. (ii) As the building block size (nanoparticle diameter) of the hierarchically hollow nanocubes is so thin that reaches a scale comparable with the Debye length (electron depletion layer thickness), the complete depletion of electrons will be achieved, meaning that the amount of oxygen that can be absorbed and ionized is maximized. (iii) Relative to the traditional point-to-point contacting of neighboring spherical particles, the high probabilistic face-to-face contacting form of our nanocages exhibits a broader conductive channel of electrons between neighboring particles [15], resulting in lowering the contact potential barrier (Fig. S2, Supplementary materials). From this point of view, the reasonable porous and non-spherically hollow structure makes SnO₂ more efficient to participate in gas detection. (iv) More importantly, Pd-loaded SnO₂ nanocages exhibits the significantly improved toluene-sensing performances, which may be promoted by the additional effects of Pd [17,35–37]. Gen-

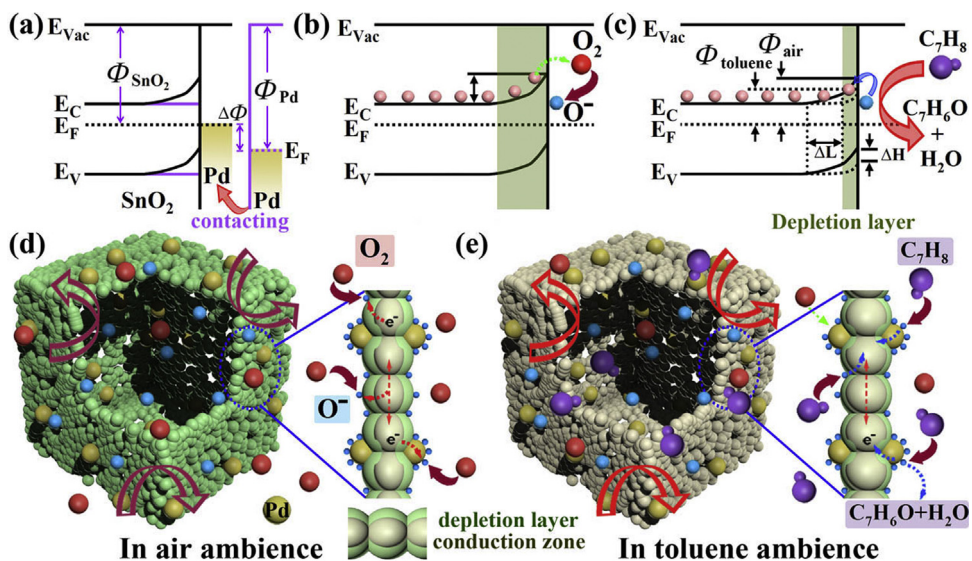


Fig. 10. Schematic energy band diagrams of a SnO₂ and Pd contact (a) with establishing the contact, with being exposed to (b) air and (c) toluene ambience, respectively. (d) and e) Schematic diagrams of possible gas sensing mechanisms of Pd-loaded SnO₂ porous cages.

erally, compared with unloaded SnO₂, the loaded Pd nanoparticles are known to be responsible for enhancement of sensing performances through two main aspects. The first aspect is based on the improved catalytic activity of Pd (PdO) to oxygen dissociation, which can greatly increase the molecule-ion conversion rate and the quantity of adsorbed oxygen ions, resulting in the faster and greater degree of electron depletion of Pd-loaded SnO₂ than that of unloaded SnO₂ and eventually enhancing sensing reaction and performances. Another aspect is related with the spillover effect, which plays an important role in the interface interactions [17]. The vacant sites for adsorption on PdO will physically adsorb toluene molecules on PdO and simultaneously spillover onto the surface of SnO₂, activating the sensing reaction between toluene molecules and oxygen species and eventually improving the response. Thus, besides the hollow and porous structural merits, the additional effects of loaded Pd on the whole sensing process further improve the sensing performances for gas detection.

4. Conclusions

In summary, pure and Pd-loaded SnO₂ cubic nanocages have been successfully prepared via a multi-step route without employing any additional templates, surface modification or capping agents. The characteristic results confirm that SnO₂ nanocages exhibit cubic shape and hierarchically hollow structure which consists of nanoparticle-assembled and porous single-layered shells. The synthetic step-dependent morphology and structure evolution confirm that the formation of SnO₂ cubic nanocages is addressed in terms of the phase transition from initial ZHS templates to hybrid Zn₂SnO₄/SnO₂ and entire evacuation of Zn₂SnO₄ phase due to the differential stability in acid etching. Furthermore, the effects of the Pd-loaded amount on toluene sensing performances have also been investigated and the results demonstrate that Pd-loaded SnO₂ nanocages exhibit low working temperature, low detection limit, high response, and fast response speed, which can be mainly ascribed to sensitized action of Pd nanoparticles.

Acknowledgements

This research work was financially supported by the Natural Science Foundation of China (Grant nos. 51372095, 51402122, and 61376122), the Postdoctoral Science Foundation of China (nos.

2014T70287), the Research Fund for the Doctoral Program of Higher Education of China (no. 20120061120039), and Independent Project of State Key Laboratory of Applied Optics, Changchun Institute of Optics, Fine Mechanics and Physics, Chinese Academy of Sciences.

Appendix A. Supplementary data

Supplementary data associated with this article can be found, in the online version, at <http://dx.doi.org/10.1016/j.snb.2016.10.024>.

References

- [1] T. Seiyama, A. Kato, K. Fujushi, M. Nagatani, A new detector for gaseous components using semiconductive thin films, *Anal. Chem.* 34 (1962) 1502.
- [2] N. Yamazoe, G. Sakai, K. Shimanoe, Oxide semiconductor gas sensors, *Catal. Surv. Asia* 7 (2003) 63–75.
- [3] X.M. Chen, Toxicology review of toluene, *Chin. J. Ind. Hyg. Occup. Dis.* 5 (1984) 291–295.
- [4] L.L. Wang, Z. Lou, T. Fei, T. Zhang, Zinc oxide core-shell hollow microspheres with multi-shelled architecture for gas sensor applications, *J. Mater. Chem.* 21 (2011) 19331–19336.
- [5] Y. Zeng, T. Zhang, L.J. Wang, M.H. Kang, H.T. Fan, R. Wang, Y. He, Enhanced toluene sensing characteristics of TiO₂-doped flowerlike ZnO nanostructures, *Sens. Actuators B* 140 (2009) 73–78.
- [6] S.H. Wei, Y. Zhang, M.H. Zhou, Toluene sensing properties of SnO₂–ZnO hollow nanofibers fabricated from single capillary electrospinning, *Solid State Commun.* 151 (2011) 895–899.
- [7] J.L. Tian, J. Wang, Y.W. Hao, H.Y. Du, X.G. Li, Toluene sensing properties of porous Pd-loaded flower-like SnO₂ microspheres, *Sens. Actuators B* 202 (2014) 795–802.
- [8] F.H. Zhang, X.H. Wang, J.P. Dong, N. Qin, J.Q. Xu, Selective BTEX sensor based on a SnO₂/V₂O₅ composite, *Sens. Actuators B* 186 (2013) 126–131.
- [9] G.J. Li, X.H. Zhang, S. Kawi, Relationships between sensitivity, catalytic activity, and surface areas of SnO₂ gas sensors, *Sens. Actuators B* 60 (1999) 64–70.
- [10] L.P. Qin, J.Q. Xu, X.W. Dong, Q.Y. Pan, Z.X. Cheng, Q. Xiang, F. Li, The template-free synthesis of square-shaped SnO₂ nanowires: the temperature effect and acetone gas sensors, *Nanotechnology* 19 (2008) 185705.
- [11] Y. Shimizu, T. Hyodo, M. Egashira, Mesoporous semiconducting oxides for gas sensor application, *J. Eur. Ceram. Soc.* 24 (2004) 1389–1398.
- [12] Y.L. Wang, X.C. Jiang, Y.N. Xia, A solution-phase, precursor route to poly-crystalline SnO₂ nanowires that can be used for gas sensing under ambient conditions, *J. Am. Chem. Soc.* 125 (2003) 16171–16176.
- [13] Y.E. Chang, D.Y. Youn, G. Ankonina, D.J. Yang, H.G. Kim, A. Rothschild, I.D. Kim, Fabrication and gas sensing properties of hollow SnO₂ hemispheres, *Chem. Commun.* 45 (2009) 4019–4021.
- [14] L.L. Wang, Z. Lou, T. Zhang, H.T. Fan, X.J. Xu, Facile synthesis of hierarchical SnO₂ semiconductor microspheres for gas sensor application, *Sens. Actuators B* 155 (2011) 285–289.

- [15] Y.F. Bing, Y. Zeng, C. Liu, L. Qiao, W.T. Zheng, Synthesis of double-shelled SnO₂ nano-polyhedra and their improved gas sensing properties, *Nanoscale* 7 (2015) 3276–3284.
- [16] J.H. Lee, Gas sensors using hierarchical and hollow oxide nanostructures: overview, *Sens. Actuators B* 140 (2009) 319–336.
- [17] N. Yamazoe, New approaches for improving semiconductor gas sensors, *Sens. Actuators B* 5 (1991) 7–19.
- [18] J. Mizsei, J. Harsányi, Resistivity and work function measurements on Pd-doped SnO₂ sensor surface, *Sens. Actuators* 4 (1983) 397–402.
- [19] J.G. Duh, J.W. Jou, B.S. Chiou, Catalytic and gas sensing characteristics in Pd-doped SnO₂, *J. Electrochem. Soc.* 136 (1989) 2740–2747.
- [20] Y.C. Lee, H. Huang, O.K. Tan, M.S. Tse, Semiconductor gas sensor based on Pd-doped SnO₂ nanorod thin films, *Sens. Actuators B* 132 (2008) 239–242.
- [21] G. Korotcenkov, V. Brinzari, Y. Boris, M. Ivanov, J. Schwank, J. Morante, Influence of surface Pd doping on gas sensing characteristics of SnO₂ thin films deposited by spray pyrolysis, *Thin Solid Films* 436 (2003) 119–126.
- [22] M.V. Vaishampayan, R.G. Deshmukh, I.S. Mulla, Influence of Pd doping on morphology and LPG response of SnO₂, *Sens. Actuators B* 131 (2008) 665–672.
- [23] H. Zhang, Z. Li, L. Liu, X. Xu, Z. Wang, W. Wang, W. Zheng, B. Dong, C. Wang, Enhancement of hydrogen monitoring properties based on Pd-SnO₂ composite nanofibers, *Sens. Actuators B* 147 (2010) 111–115.
- [24] S.W. Choi, A. Katoch, G.J. Sun, S.S. Kim, Bimetallic Pd/Pt nanoparticle-functionalized SnO₂ nanowires for fast response and recovery to NO₂, *Sens. Actuators B* 181 (2013) 446–453.
- [25] Y. Zeng, L. Qiao, Y.F. Bing, M. Wen, B. Zou, W.T. Zheng, T. Zhang, G.T. Zou, Development of microstructure CO sensor based on hierarchically porous ZnO nanosheet thin films, *Sens. Actuators B* 173 (2012) 897–902.
- [26] D. Andreeva, T. Tabakova, V. Idakiev, P. Christov, R. Giovanoli, Au/α-Fe₂O₃ catalyst for water-gas shift reaction prepared by deposition-precipitation, *Appl. Catal. A* 169 (1998) 9–14.
- [27] R.I. Eglitis, M. Rohlfing, First-principles calculations of the atomic and electronic structure of SrZrO₃ and PbZrO₃ (001) and (011) surfaces, *J. Phys.: Condens. Mater.* 22 (2010) 415901.
- [28] Z.L. Wang, Transmission electron microscopy of shape-controlled nanocrystals and their assemblies, *J. Phys. Chem. B* 104 (2000) 1153–1175.
- [29] V.R. Shinde, T.P. Gujar, C.D. Lokhande, Enhanced response of porous ZnO nanobeads towards LPG: effect of Pd sensitization, *Sens. Actuators B* 123 (2007) 701–706.
- [30] L. Liu, Y. Zhang, G.G. Wang, S.C. Li, L.Y. Wang, Y. Han, X.X. Jiang, A.G. Wei, High toluene sensing properties of NiO-SnO₂ composite nanofiber sensors operating at 330° C, *Sens. Actuators B* 160 (2011) 448–454.
- [31] H.H. Li, F.L. Meng, J.Y. Liu, Y.F. Sun, Z. Jin, L.T. Kong, Y.J. Hu, J.H. Liu, Synthesis and gas sensing properties of hierarchical meso-macroporous SnO₂ for detection of indoor air pollutants, *Sens. Actuators B* 166–167 (2012) 519–525.
- [32] Q. Qi, T. Zhang, L. Liu, X.J. Zheng, Synthesis and toluene sensing properties of SnO₂ nanofibers, *Sens. Actuators B* 137 (2009) 471–475.
- [33] N. Yamazoe, J. Fuchigami, M. Kishikawa, T. Seiyama, Interactions of tin oxide surface with O₂, H₂O and H₂, *Surf. Sci.* 86 (1979) 335–344.
- [34] M. Egashira, Y. Shimizu, Y. Takao, S. Sako, Variations in I-V characteristics of oxide semiconductors induced by oxidizing gases, *Sens. Actuators B* 35 (1996) 62–67.
- [35] S.W. Choi, S.S. Kim, Room temperature CO sensing of selectively grown networked ZnO nanowires by Pd nanodot functionalization, *Sens. Actuators B* 168 (2012) 8–13.
- [36] Y. Shen, T. Yamazaki, Z. Liu, D. Meng, T. Kikuta, N. Nakatani, M. Satio, M. Mori, Microstructure and H₂ gas sensing properties of undoped and Pd-doped SnO₂ nanowires, *Sens. Actuators B* 135 (2009) 524–529.
- [37] A. Kolmakov, D.O. Klenov, Y. Lilach, S. Stemmer, M. Moskovits, Enhanced gas sensing by individual SnO₂ nanowires and nanobelts functionalized with Pd catalyst particles, *Nano Lett.* 5 (2005) 667–673.

Biographies

Liang Qiao is an associate professor at the College of Science, Changchun University, China. She received her PhD degree from the Department of Materials Science, Jilin University, China in 2007. Now, she is engaged in the gas sensing properties of semiconducting functional materials, and graphene nanocomposites.

Yifei Bing received his BE degree from the Department of Materials Science, Jilin University, China in 2010. Now he is working for his PhD degree, majoring in Materials Physics and Chemistry, in Jilin University. He is interested in the synthesis and applications of graphene composites, functional nanomaterials, and gas sensors.

Yanzhe Wang is working for his PhD degree, majoring in Materials Physics and Chemistry, in Jilin University. He is interested in the synthesis and applications of semiconducting oxides with hollow and porous structures.

Shansheng Yu is an associate professor at the Department of Materials Science, Jilin University, China. He received his PhD degree from the Department of Materials Science, Jilin University, China in 2007. Now, he is engaged in the simulation of the gas sensing properties of semiconducting functional materials, and graphene nanocomposites.

Zhongzhu Liang is a professor in State Key Laboratory of Applied Optics, Changchun Institute of Optics, Fine Mechanics and Physics, Chinese Academy of Sciences. He received his PhD degree from State Key Laboratory of Superhard Materials, Jilin University, China in 2007. Now, he is engaged in micro optical electro-mechanical-system, plasmonics and sensors.

Yi Zeng received his MS degree from State Key Laboratory of Superhard Materials, Jilin University, China in 2007. He received his PhD degree from College of Electronic Science and Engineering, Jilin University, China in 2010 majored in microelectronics and solid state electronics. He was appointed the associate professor in Department of Materials Science, Jilin University in October, 2012. Now, he is engaged in the synthesis and characterization of the semiconducting functional materials, nanocomposites, and gas sensors.